Electrodeposition and isothermal aging of Co and Mn layers on stainless steel for interconnectors: Initial stages of spinel phase formation

R. Pinto [a,*], M.J. Carmezim [a,b], M.F. Montemor [a]

[a] ICEMS, Instituto Superior Técnico, Universidade de Lisboa, Av. Rovisco Pais 1, 1049-001 Lisboa, Portugal
[b] Instituto Politécnico de Setúbal, ESTSetúbal, DEM, Portugal

HIGHLIGHTS

- Electrodeposited Co and Mn layers were annealed to obtain an oxide coating.
- Structural and chemical analysis of early stages of transformation is reported.
- Spinel phase formation was achieved in both oxidizing and neutral atmosphere.
- Co and Mn diffusion and counter-diffusion was tracked up to 1 h exposure.
- No Cr from the stainless steel substrate was detected in the coating.

ARTICLE INFO

ABSTRACT

Electrodeposited Co and Mn spinel phase oxides for application as coatings for metallic interconnectors in Solid Oxide Fuel Cells were prepared. The study aims at understanding the initial stages of transformation of the metallic layers into the spinel phase. Co and Mn metallic layers were sequentially deposited over AISI 430 stainless steel substrate from acidic sulfate solutions and annealed in oxidizing and inert atmospheres between 600 °C and 800 °C. The coatings obtained showed a thickness above 20 μm. After 1 h of isothermal aging the coatings were composed of layers of un-reacted metallic elements and Mn based oxides. The spinel phase was studied by XRD and revealed Mn based tetragonal structure Mn_3O_4 with Co in solid solution and a non-determined Co/Mn ratio. According to EDS measurements this ratio should vary with depth. Full conversion was not obtained at these time frames with the presence other Mn oxides (MnO and Mn_2O_3). In inert atmosphere, the allotropic Mn transformation from α to β phase was detected. No outward diffusion of Cr was detected, due to the short exposure times.

© 2014 Elsevier B.V. All rights reserved.

1. Introduction

Recent trends in new electrolytes for Solid Oxide Fuel Cells (SOFCs) have shown that it is possible to reduce the operating temperatures into the 600–800 °C range [1–3]. Thus, some ceramic based materials can be replaced by cheaper metallic components. The interconnect layer is a prime candidate for such replacement. Interconnectors (ICs) are responsible for the physical separation of anode and cathode and for electrical contact between individual cells in a stack, as cell stacking is essential for increasing power density. The IC materials must comply with strict requirements:

- complete density to block gas crossover between anodic and cathodic layers;
- chemical stability at high temperatures and reduced chemical reactions with the materials comprising the cathode (oxidizing atmosphere) and the anode (reducing atmosphere);
- low area specific resistance (ASR), which should not increase during operation;
- coefficient of thermal expansion (CTE) matching the other cell components;
- adequate mechanical strength and creep resistance;
- good thermal conductivity.

The most suitable metallic alloys for this purpose are stainless steels and Cr or Ni based alloys [4]. Ferritic stainless steels (FSSs)

* Corresponding author. Tel.: +351 218417234; fax: +351 218419771.
  E-mail address: ricardo.a.pinto@tecnico.ulisboa.pt (R. Pinto).

have shown, so far, the best compromise regarding the required properties.

Regarding the CTE, FSSs vary in the range of 9 to $11 \times 10^{-6} K^{-1}$ [4], which is a near perfect match with the ceramic components of a SOFC, namely, lanthanum and strontium doped manganite perovskites (LSM) cathodes [5] and the yttria stabilized zirconia (YSZ) electrolytes [6]. Ni based alloys and other types of stainless steels present unacceptably high CTE values, even though a slightly higher CTE of the IC is desirable to maintain ceramic components under compressive stress.

The application of FSSs and Cr based alloys as ICs has a major drawback associated with the volatilization and release of Cr compounds from chromia scales. In the presence of water vapor, Cr oxy-hydroxides species such as $CrO_2(OH)_2$ can be formed (although the exact composition depends on temperature and vapor pressure [4]) that have the capability of migrating through several layers of the cell. This mechanism is known as Cr poisoning and it is felt mostly on the cathode/electrolyte interface (vapor pressures are higher in the air electrode), where these species are eventually reduced and create deposits that deteriorate cell performance by blocking ion flow and reducing electroactive area of the electrode.

The two strategies put forward in literature as possible solutions addressing the problem of Cr poisoning are alloy development and coating technologies. These have been the subject of recent reviewing [7] in which the formation of spinel phase coatings by electrodeposition (EDP) followed by oxidation seems to be one of the most promising approaches. The oxides formed show suitable conductivity and potential for keeping low oxidation rates, suppressing sub-scale growth and blocking diffusion of Cr compounds. The method itself is not expensive, simple and easy to apply over different shapes. The spinel phases from the Cu–Mn and Co–Mn show the highest levels of conductivity [8] and are, currently, the prime candidates for spinel phase coatings.

The usual approach is the simultaneous co-deposition of both elements from solutions containing the two cations [9,10], and the co-deposition with rare-earth particles to increase corrosion resistance [11], but studies on the deposition of separate metallic layers can also be found in literature [12].

Recent advances have been published on the interaction between chromia and spinel oxides based on the Co–Mn system with varying composition and the addition doping elements [13]. The formation of a reaction layers through outward diffusion of Cr and counter-diffusion of Co and Mn was detected and suggested as beneficial for reduction of chromium volatilization. The presence of the reaction layer and doped spinel phases formed by diffusion was also confirmed on coatings applied by slurry on a FSS substrate [14]. The subscales were found to be composed by two distinct phases: a continuous chromia layer and small pockets of cubic Mn–Cr spinel phase situated between the chromia and the substrate. The same subscale structure was detected in Co coated FSS, with a coating applied by PVD technique [15].

In this work, we investigate the formation of separate metallic layers (cobalt and manganese) by EDP, and formation of the spinel phase by interdiffusion of the elements during oxidation. In particular, the study focus on the initial stages of formation of coatings with single oxide layer of spinel phase with a general formula of $(CoMn_3)O_4$. During these early stages compositional and structural changes are likely to occur, relevant to coating behavior but still not fully understood.

2. Experimental

2.1. Materials, solutions and conditions for EDP

Coupons were cut from AISI 430 stainless steel (SS) sheets as received (annealed). Prior to electrodeposition (EDP), the coupons were degreased in ultrasonic acetone bath. A surface preparation known as *strike plating* was adapted from literature [11], and was carried at 25 °C for 5 min. The EDP solutions were sulfate based and the experiments were performed at 40 °C with magnetic stirring at 500 rpm. Electrolyte composition was also adapted from literature [11,16–18] and set at 400 g L^{-1} $CoSO_4.7H_2O$ and 35 g L^{-1} H_3BO_4 for the Co solution, while the Mn solution was prepared from 210 g L^{-1} $MnSO_4.H_2O$ and 120 g L^{-1} $(NH_4)_2SO_4$. The EDP experiments were performed at pH 4, adjusted with diluted H_2SO_4, diluted NaOH (Co solution) or NH_4OH (Mn solution). All solutions were prepared with Millipore® water.

Both electrodes (anode and cathode) were placed in the same cell in a vertical position at a distance of approximately 1 cm. Co strike plating and EDP were performed with sacrificial anodes of commercially pure Co and a graphite anode was used for Mn EDP. Co and Mn EDP current densities were set at 100 mA cm^{-2} and 200 mA cm^{-2}, respectively, for an EDP area of approximately 9 cm^2. Co and Mn layers were deposited sequentially, first Co over the substrate and then Mn over Co, with a deposition time of 5 min per layer.

2.2. Annealing procedure

Samples were subjected to isothermal cycling for 10 min and 1 h in two different atmospheres: air and N_2. A Carbolite STF tubular furnace with a Eurotherm 808 controller was used for this experimental stage and three temperatures were experimented and controlled by means of a thermocouple: 600 °C, 700 °C and 800 °C.

2.3. Sample characterization

Weight evolution of the samples was measured at different experimental steps with a Metler AE 166 scale.

Electron microscopy was performed with a JEOL 7001-F device equipped with field emission gun and an Oxford INCA unit for energy dispersive X-ray spectroscopy. Images were obtained in secondary electrons and back-scattered electrons mode of topography and cross-section, which were complemented with chemical analysis.

The crystalline phases were studied by X-ray diffraction (XRD) with a Bruker D8 ADVANCE apparatus in Bragg-Brentano geometry and a Cu anode at 40 kV acceleration voltage and 40 mA of current. Measurements were taken in a 2θ range of 15°–65° with step size of 0.04° and 3 s of step time.

3. Results and discussion

3.1. Electrodeposited layers

The surface topography of samples submitted to strike plating is presented in Fig. 1 (top). The anodic activation step of the process, in which the SS was subjected to positive currents, provoked dissolution of material and the creation of a rough surface. A material with strand like morphology was homogeneously formed over the surface. EDS analysis revealed that it was composed of cobalt deposited during the second stage when negative currents were applied. Sub-micrometer carbides were also visible as rod-like features protruding from the surface at ×20000 magnification. The small current densities applied during strike plating did not allow the formation of thick Co layers, but the Co strands and rough morphology are expected to improve deposition and adhesion of the next Co EDP layer.

The surface topography after EDP of Co and Mn is shown in Fig. 1 (bottom). After strike plating, Co EDP created a homogeneous grain structure throughout the surface with somewhat elongated grains,
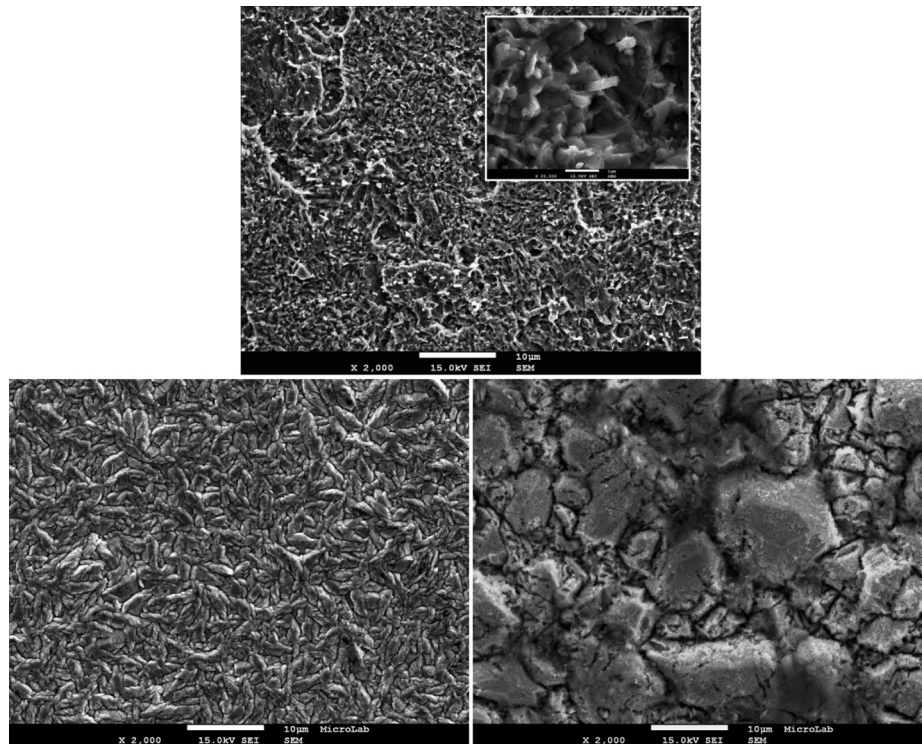
Fig. 1. SEM micrographs of steel surface at ×2000 magnification: after strike plating—top (×20000 standout), after Co EDP (low left) and after Mn EDP (low right).

approximately 1 μm wide and 3–4 μm long. The Mn layer, which was electrodeposited on top of the Co layer, showed a higher level of disorder with larger grains growing up to 10 μm in diameter. EDS analysis of EDP Co revealed only trace amounts of iron from the substrate, while in the EDP Mn layer, no traces of Co (the layer immediately bellow) were detected. The EDP Mn layer also revealed a higher oxygen content (approximately 12% wt).

The cross-section analysis depicted in Fig. 2 revealed a thickness of approximately 9.5 μm and 14.8 μm, for EDP layers Co and Mn respectively, with some heterogeneity in the Mn layer. The porosity of the coating was not quantified.

The XRD results revealed the presence of only one crystalline phase that was identified as α-Mn (ICDD 65-3159), with peaks at 2θ angles: 40.52°, 43.12°, 47.84°, 50.00° and 52.44°; indexed for planes (400), (411), (332), (422) and (510), respectively. The body centered cubic α phase is the most common phase obtained by electrode-position [19]. The combination of this result with SEM-EDS revealed that the oxygen detected in the chemical analysis did not arise from the presence of crystalline Mn oxides; the signal probably resulted from the presence of amorphous oxides. The absence of diffraction peaks from the Co layer or the SS substrate should be caused mainly by X-ray absorption from the elements present, in accordance with the mass absorption coefficients published in literature [20]. All the main elements present in our system (Mn, Co, Fe and Cr) have high coefficients regarding the Cu kα radiation (wavelength of 1.54 Å) indicating high absorption. Co has a particularly high absorption, being the third highest in the periodic table [20]. The loss of signal should also be increased by inelastic scattering and internal reflection. A separate XRD analysis of a single EDP Co layer (with the same conditions), revealed the deposited phase had hexagonal crystalline structure (ICDD 71-4239).

The coupons were weighed after each EDP step and the variation corrected by deposited area. Similar weight increase was measured for Co and Mn layers, leading to similar deposition rates:

$30.9 \times 10^{-6} \pm 0.3$ gcm^{-2} s^{-1} and $33.9 \times 10^{-6} \pm 3.0$ gcm^{-2} s^{-1} (mean ± 95% confidence interval, $n > 30$), for Co and Mn respectively. The fact that the weight increase during Mn EDP was only marginally higher than during Co EDP, at twice the current density, was in line with SEM observations but was also indicative of lower cathode efficiency. This result was predictable, considering the standard potentials of the elements: −0.277 V (vs. SHE) for Co and −1.179 V for Mn (vs. SHE) [21]. Cathode efficiencies for both elements were calculated from Faraday's law; while Co EDP occurred with approximately 100% efficiency, Mn EDP was only around 60%. In addition, the true efficiency of Mn EDP must be even lower, since a non-negligible amount of oxygen, that will likely also contain hydrogen, was detected in the EDS elemental analysis.
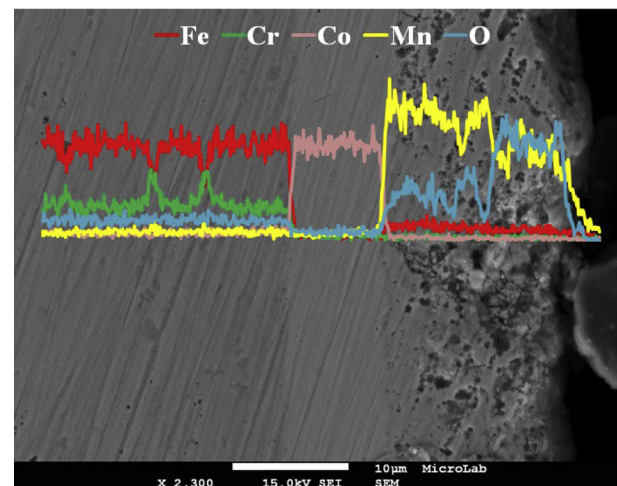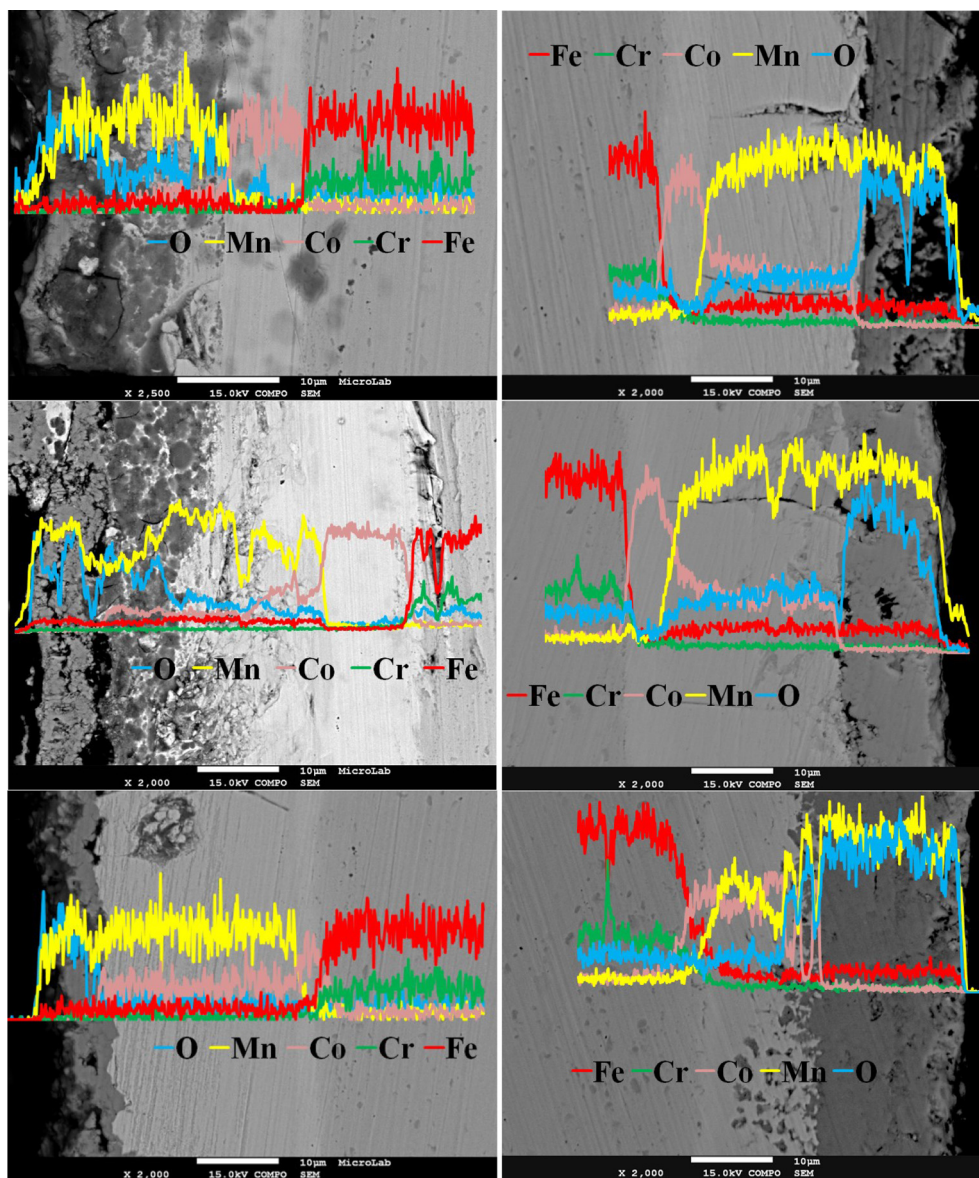

Fig. 2. SEM back-scatter cross-section micrograph of EDP layers of Co and Mn on steel surface with overlaid EDS line sweep.

Fig. 3. SEM back-scatter micrograph and EDS analysis across sample cross-section after annealing in air for 10 min (left) and 1 h (right) at different temperatures: 600 °C (top), 700 °C (center), 800 °C (low).

Calculation of the layer thickness was also performed considering sample weight increase (10.18 mg cm^{-2} and 9.26 mg cm^{-2}) and theoretical densities presented in the ICDD charts (8.84 g cm^{-3} and 7.74 g cm^{-3}), for Co and Mn respectively. The calculated thicknesses of 11.5 μm (Co) and 12.4 μm (Mn) were in good agreement with SEM measurements. While the overestimation of Co thickness can be directly attributed to the edge effect that is not accounted for in a weight measurement, the underestimated Mn value cannot be associated with a single factor; besides the edge effect, it can also result from: oxygen content (interferes with coating mass and volume), porosity and layer roughness (interferes with measurement by SEM).

3.2. Air annealing

3.2.1. SEM analysis

Surface topography (not shown) denoted intensive surface recrystallization. After 10 min of annealing the morphology was very similar at 600 °C and 700 °C containing two types of structures: homogeneous sub micrometer crystallites and scattered needle like features with approximately 3 μm in length. At 800 °C the crystallites became rounder and slightly larger. No severe cracking was visible. As annealing time was increased to 1 h, the needle type structures disappeared for all samples. At 1 h of annealing, rounder grains were visible, starting at 600 °C, which became polygonal (equiaxial) and enlarged as the temperature increased.

The cross-section images obtained in back-scattered electrons mode and chemical analysis performed through EDS line profiles (Fig. 3) revealed the presence of a multi-layered coating after oxidation at all temperatures tested, showing, in general, good interlayer adhesion.

The cross section analysis (from the substrate outward) showed a first layer composed of non-reacted cobalt, whose thickness decreased as annealing temperatures and time increased. The Co layer was visibly as a separate layer for all samples except for the 1 h annealing at 800 °C; in this case, the solubility of Co in Mn appeared to be higher than expected by the increase in temperature and was

the probable outcome of a structural modification. Mn presents four different crystalline structures: α, β, γ and δ (from low to high temperatures), resulting from three allotropic transformations. In the temperature range tested, the relevant transformation is the change from the α-phase, with body centered cubic structure (bcc) mentioned earlier to the β-phase, presenting a cubic structure (space group P4₁32). In the Co–Mn phase diagram [22], the transformation temperature for pure Mn is 710 °C and decreases with increasing Co content, creating a solid solution (αMn) with a relatively low Co solubility (approximately 2–3 wt% in the 600–700 °C range). The βMn solid solution, on the other hand, has a much higher Co solubility (maximum of 49 wt% at 545 °C), which should account for the increased diffusion detected in the EDS. Another indication that the phenomenon was structure related was the fact that diffusion of Co into the substrate, although higher, did not increase at the same level. The presence of this layer limited crack propagation at the interface between the non-reacted Co and the next outward layer. Differences in CTEs within the layered coating and structural modifications occurring during thermal annealing can influence crack formation; however, in our experiments the most likely origin for cracking was the experimental procedure, whereby the samples were not allowed to cool slowly to ambient temperature but were removed to a section with lower temperature within the furnace, in order to stop the transformation at the required times. Cracks are not likely to occur in usual working conditions.

The following level was an *interdiffusion* layer of Co and Mn with different amounts of oxygen. The general trend in thickness evolution for this layer was an increase with increasing temperature. At lower temperatures (600 °C and 700 °C) the interdiffusion layer was less homogeneous and, particularly at 700 °C, there was an apparent stratification into two sub-layers (visible in image contrast and oxygen EDS signal). At higher temperatures, the homogeneity of the layer was denoted visually and by the EDS profiles of the elements (Co, Mn and O).

The outer layer in all samples was composed of oxidized Mn without any Co. At shorter annealing times the thickness decreased with increasing temperature and this external layer was also where most of coating defects such as: cracks, pores and lack of inter-layer adhesion were detected. Conversely, for 1 h of oxidation the thickness of the outer Mn–O layer increased with temperature. For temperatures of 800 °C oxide "particles" with little or no Co grew into the diffusion layer that were combined with void type defects.

A darker phase, with dimensions of approximately 1 μm, was visible in the cross sections and quite homogeneous. This phase was present prior to annealing (Fig. 2), and corresponded to increased intensity of Cr and reduction of Fe in EDS signals. It did not show any evolution with annealing time and temperature or in coating/substrate adhesion. At this short time frame, no chromia sub-scales were formed in the samples.

3.2.2. XRD results

Fig. 4 presents the diffractograms of samples annealed in air with the patterns of the phases identified, Mn and three of its oxides, which are summarized in Table 1. Similarly to the sample analyzed before annealing, and although there was a distinct layer clearly visible in the SEM-EDS cross-section results, no Co signal was detected.

After 10 min of annealing, at lower temperatures (600 °C and 700 °C) non-reacted Mn was detected with the quantity decreasing with increasing temperature. This should account for the lack of homogeneity in the interdiffusion layer discussed earlier and the phase was not present at higher temperatures. The Mn_3O_4 phase showed a strong presence at all annealing temperatures, with a maximum in stability at 800 °C. This phase should not actually correspond to pure Mn_3O_4 but rather to the mixed spinel $(MnCo)_3O_4$, with Mn and Co in solid solution. Furthermore, it is likely that the spinel is the main constituent of the interdiffusion layer, especially at 800 °C. This conclusion is supported by the EDS profiles and by the existence of a slight mismatch in 2θ angles between the chart and the experimental data. The replacement within the structure of Mn atoms by Co atoms (and vice versa), should distort the cells and cause a modification of lattice parameters.

The Mn_2O_3 phase was present at all annealing temperatures and, similarly to the spinel phase, the signal was stronger at 800 °C. It was not possible to determine the location of this phase in the coating (interdiffusion layer, external Mn–O layer or both).

The most external layer should correspond to the MnO phase, present at all annealing temperatures. It represents the lowest oxidation form of Mn and was probably the first oxide formed upon annealing.

After 1 h of annealing, no new phases were detected when compared with 10 min of oxidation. The predicted βMn phase was not detected above 700 °C, neither at 10 min nor at 1 h of oxidation. The most likely explanation is that Mn reacted very quickly and was already incorporated into oxides. It is also possible that some non-reacted phase was present at the inner part of the coating, whose signal would be shielded by the oxides and Co that had already diffused outwards. The Mn_2O_3 phase was only stable up to 700 °C, while at 10 min of oxidation it was present at 800 °C; this indicated its initial formation requires some time and that it was afterward converted to another phase, probably the spinel phase. Peak intensity for the spinel phase was similar at all temperatures. These results are in good agreement with literature [12,22], including the presence of MnO predicted by the Mn–O phase diagram [23]. This diagram shows large homogenous regions of defective manganosite $(Mn_{1-x}O)$ in equilibrium with either αMn or βMn, depending on weather the temperature is bellow or above the allotropic transformation temperature (706.9 °C). Manganosite is stable up to 0.5 M fraction of oxygen, with the oxidation of Mn^{2+} to Mn^{3+} and the formation of the respective cationic vacancies to balance the charge, after which the increase in oxygen content leads to the formation of oxides with ever increasing Mn oxidations states: Mn_3O_4, Mn_2O_3 and MnO_2.

The results show that the spinel phase formed was the tetragonal structure, and not the cubic one, commonly reported for higher Co contents [12]. The Mn spinel with tetragonal structure is stabilized by a phenomenon known as Jahn-Teller distortion where Mn^{3+} ions occupy octahedral sites [24]. This structure is expected to transform for longer times as the result of Co and Mn interdiffusion and the collapse of the structure into its cubic form. This may happen in a sequence similar to that found in the ICDD database: from body centered tetragonal forms Mn_3O_4 (ICDD 24-0734) and $CoMn_2O_4$ (ICDD 77-0471) to the face centered cubic Co_2MnO_4 (ICDD 84-0482). Therefore, for shorter times changes in the spinel stoichiometry and crystalline structure may occur with depth.

The analysis of the separate Co–Mn [22] and Mn–O [23] phase diagrams instead of the Mn–Co–O [12] diagram allowed the understanding of the initial reactions in this system, since these occur through diffusion and counter-diffusion across Co–Mn and Mn–O interfaces established in the EDP process.

The XRD results suggest that void type defects and apparent lack of adhesion of the outermost oxide layer, mentioned in the previous section, resulted from different structural changes occurring simultaneously at different points in the coating. The oxidation of Mn occurs with significant alterations of lattice dimensions, comprising cell contraction followed by cell expansion, as oxidation state increases (see Table 1). The interruption of annealing procedure at short times, before a complete coating conversion, into
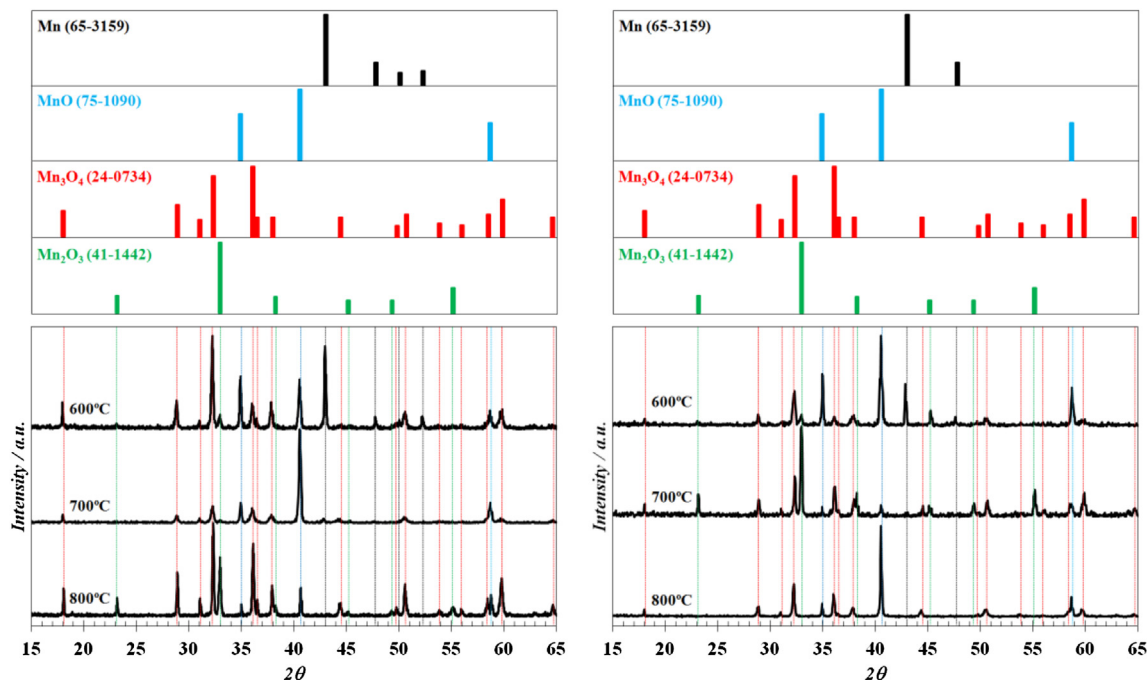
Fig. 4. X-ray diffraction results and phase identification of samples annealed in air: 10 min (left) and 1 h (right).

hausmannite phase for example, implies the cooling of adjacent grains of different phases and with dissimilar CTEs, resulting in loss of interface coherence and the formation of voids within the coating. The fact that voids were only visible at 800 °C was most likely related with reduced amounts of non-reacted Co and the disappearance of metallic Mn, whose presence at lower temperatures should allow for a better dissipation of thermal stress.

The dark phase detected in the substrate could not be structurally identified by XRD, being bellow the detection limit. However, the morphology and chemical analysis of the phase are consistent with Cr or Fe–Cr carbides usually described in this type of steel and corresponding thermal processing [25]; specifically, the $(FeCr)_{23}C_6$ with fcc crystal structure that is formed in the 500°-950 °C range, and especially in the 650–700 °C interval. The formation of carbides is known to reduce the corrosion resistance of uncoated stainless steels. However, the influence on the performance of coated systems or in cathode degradation by *chromium poisoning* is largely unknown, and no conclusions can be extrapolated from the results presented in this work.

3.3. N₂ annealing

3.3.1. SEM analysis

Regarding topography (not shown), the general trend found was an increase in crystallite size with increasing temperature and annealing time. Crystallites were sub-micrometric for all samples and presented a polygonal (almost cubic) aspect, with the

exception of the sample annealed for 1 h at 800 °C where grains were rounder.

The EDS profiles (Fig. 5) revealed a three layer structure for the coatings annealed in N₂, in general similar to the air annealed ones, comprising an un-reacted Co inner layer, an intermediate Co–Mn interdiffusion layer and an outward Mn–O layer. The results account for a decreased thickness of the inner Co layer and of the outer Mn–O layer with increasing annealing temperature and time, while the interdiffusion layer showed an opposite trend. The interdiffusion layer, at shorter annealing times, presented two distinct sub-layers at lower temperatures; these sub-layers seemed to result from an incomplete interdiffusion process a conclusion derived from the homogeneous layer present at 800 °C. The results also confirmed the increased solubility of Co in Mn in neutral atmosphere and the persistence, at these time frames, of an oxidized Mn phase. Some diffusion of Co towards the substrate and of Fe and Cr towards the outer layer was also verified, although no Cr was detected in the interdiffusion layer or beyond.

While the void type structures visible at 800 °C were similar to the ones reported for air annealing, the outermost oxide layer seemed to suffer from loss of adhesion. This was probably the result of limited inward diffusion of oxygen due to lower oxygen pressure in the atmosphere. As oxygen was hindered from diffusion out of the external layer, outward diffusion of Co into the external layer, that would improve adhesion, was also blocked. The layer became chemically more dissimilar and less capable of responding to the stress generated during the fast cooling stage.

3.3.2. XRD results

Despite the similarities in layered structures observed in different atmospheres, the XRD results (Fig. 6) suggested a different nature. At 10 min of annealing, the first noticeable feature was the reduction in the signal of the higher oxidation states of Mn oxides: the spinel phase was not detected (or it was reduced to vestigial amounts) and the Mn_2O_3 phase was not detected in any sample. The two main phases present were Mn and MnO; while the Mn signal reduces with increasing temperature, the MnO signal increases with

Table 1
Phases detected after annealing in air.

| Phase	Composition	ICDD chart	Space group	Lattice	Parameters (nm)
αMn	Mn	65-3159	I$\bar{4}$3m	bcc	$a = 8.9131$
Manganosite	MnO	75-1090	Fm$\bar{3}$ m	fcc	$a = 4.4460$
α-Hausmannite	α-Mn₃O₄	24-0734	I4₁/amd	bct	$a = 5.7621$
					$c = 9.4696$
β-Bixbyte	β-Mn₂O₃	41-1442	Ia$\bar{3}$	bcc	$a = 9.4901$
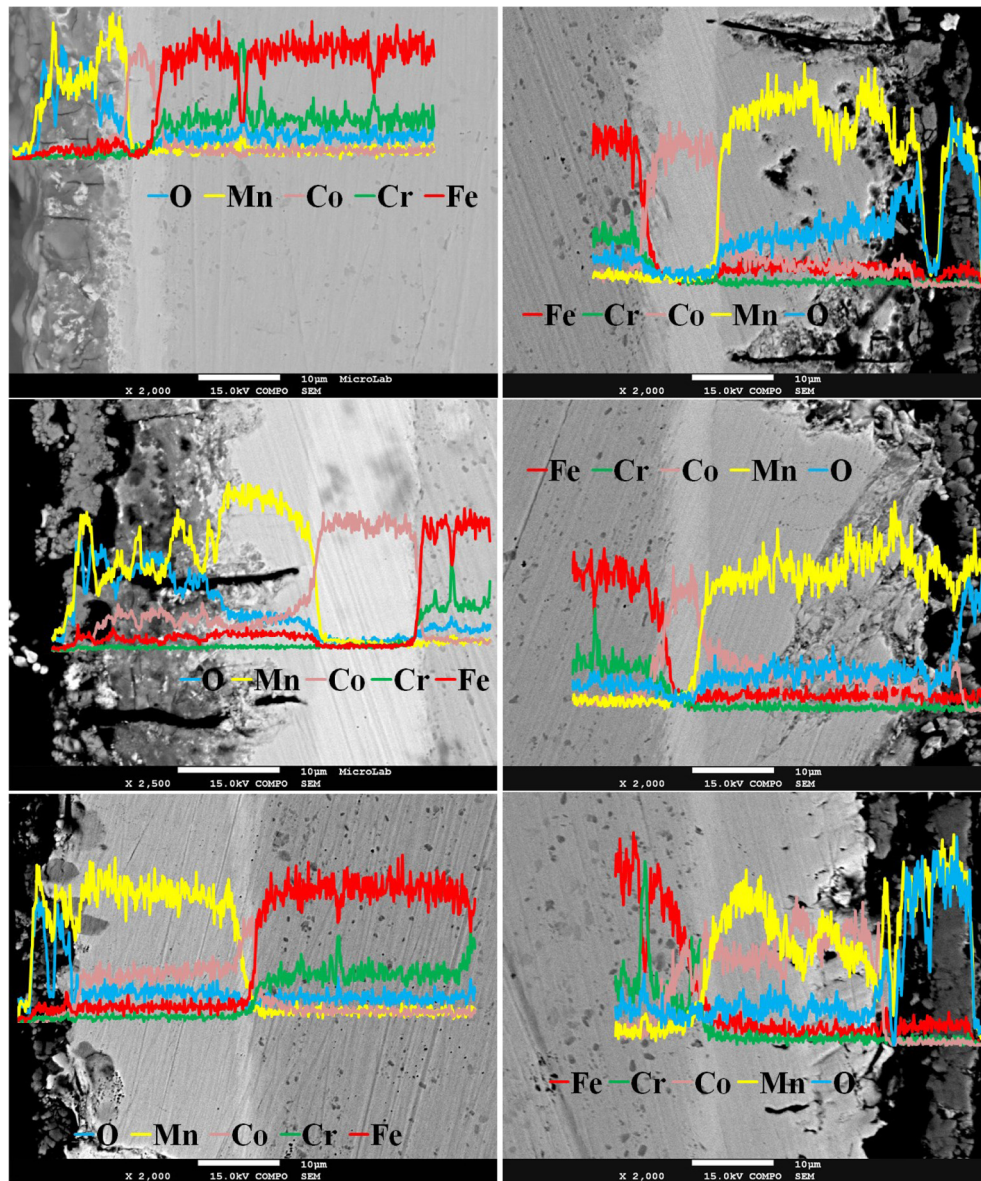
Fig. 5. SEM back-scatter micrograph and EDS analysis across sample cross-section after annealing in N_2 for 10 min (left) and 1 h (right) at different temperatures: 600 °C (top), 700 °C (center), 800 °C (low).

increasing temperature. The decrease of the Mn signal seems in contradiction with SEM-EDS results. Based on the SEM and XRD results, the logical attribution of the layers would be an inner non-reacted Co layer (not detected in XRD for the reasons stated already stated above), interdiffusion layer of Mn and Co with small quantities of Mn_3O_4 and an outer layer comprised of MnO. However, neither the evolution of MnO, or Mn_3O_4 for that matter, justify the absence of the metallic Mn signal, whose layer thickness increased with temperature. The results obtained support the statement that this was the result of a shielding effect of Co, interdiffused in the Mn layer, and the outer oxides. Finally, the annealing conditions also provoked the change in Mn crystalline structure predicted earlier: at 700 °C (a temperature lower than predicted by the phase diagrams [22,23]) the Mn structure changed from the bcc α-phase, present after electrodeposition and air annealing, to the cubic β-Mn phase (ICDD 33-0887, spatial group $P4_132$), with larger Co solubility. Several differences denoted the alteration: shift of the two main peaks in the αMn (43.016° and 47.823°) to lower 2θ angles (42.995°

and 47.754°) now belonging to crystallographic planes (221) and (311), respectively; the appearance of a new strong peak (second in intensity) at 45.404° for plane (310); the disappearance of lower intensity peaks at 50.092° and 52.289°, replaced by peaks 31.674° and 54.342° for planes (210) and (321), in that order.

After 1 h of annealing in N_2 atmosphere, the XRD diffractograms showed a reduced presence of the Mn phase at lower temperatures (600 °C and 700 °C), denoted by the presence of a single peak, the most intense. From comparison with the 10 min results, it's possible to conclude that at 600 °C the phase present was the α phase, while at 700 °C was probably the β phase. However, a concluding iden- tification could not be obtained since the only peak present was at an angle common to both the α and β phase. The diffractogram for 800 °C annealing indicated the presence of both MnO and spinel phase in amounts which, qualitatively, appeared to be similar.

In the XRD results and regardless of temperature or atmosphere, there was an inversion in peak intensity in the spinel phase for the two strongest peaks: plane (211) at 36.094° always presented a
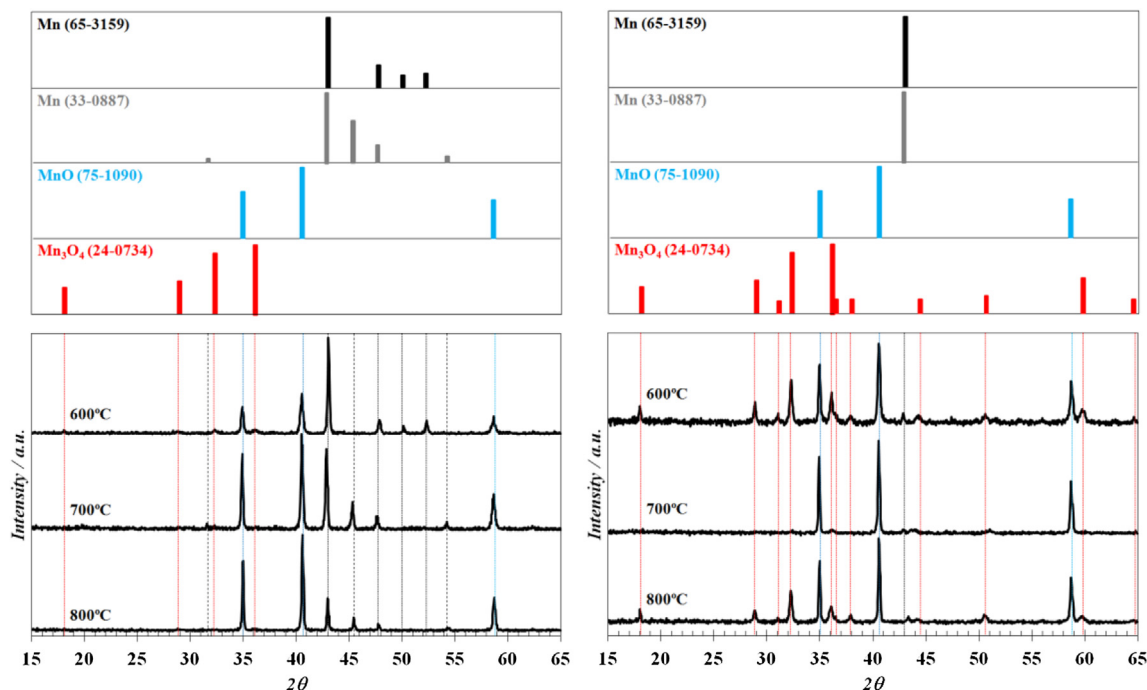
Fig. 6. X-ray diffraction results and phase identification of samples annealed in N_2: 10 min (left) and 1 h (right). (For interpretation of the references to color in this figure legend, the reader is referred to the web version of this article.)

lower intensity than and plane (103) at 32.312°. This result suggests preferential growth along the second plane for these experimental conditions.

The mechanism proposed for void formation in air annealing (Section 3.2.2) can also explain the same phenomenon in N_2. However, the presence of β-Mn phase above 700 °C can also be taken into account, as the allotropic transformation from α-Mn ($a = 0.89139$ nm) to β-Mn ($a = 0.6319$ nm–0.6282 nm, with increasing Co content [22]) causes a significant reduction of the lattice parameter.

In neutral atmosphere, the conversion to a full spinel phase was not obtained. The full conversion to a spinel phase would result in higher conductivity, especially with the mixed $(CoMn)_3O_4$ cubic phase, as reported by Petric and co-workers [8]. However, the increased solubility of Co in Mn in N_2 atmosphere, resulting from the allotropic transformation of Mn, opens the possibility of designing a two step annealing procedure, with an initial stage in inert atmosphere and a subsequent oxidation step that could improve coating properties.

4. Conclusions

The method of electrodeposition of separate Mn and Co layers followed by annealing was successful in producing the spinel phase in both oxidizing and neutral atmospheres.

In neutral atmosphere metallic Mn was detected, at 10 min of annealing, denoting an allotropic transformation between 600 °C and 700 °C from the α to the β phase. The intensity of the XRD peaks for this phase decreases with increasing temperature associated to an increase of MnO and spinel oxide phases. After 1 h of annealing the metallic manganese phase was almost completely converted to oxide form, namely the spinel phase. These results were consistent with composition depth profiling where Co and Mn interdiffusion was observed.

In oxidizing atmospheres, the Mn phase was visible at 600 °C, being completely oxidized not only to MnO and spinel phase, but

also to Mn_2O_3 phase, independently of the oxidation time. However, increasing annealing time and temperature promoted the formation of the spinel phase. Depth profiling revealed interdiffusion of Co (outward) and Mn (inward) as observed for the neutral atmosphere. However, the Co diffusion towards the substrate seemed to increase and the onset of outward Fe diffusion was also apparent. The spinel phase formed is likely to present the general formula $(CoMn)_3O_4$, with a composition that varies with depth (higher Mn content close to the surface). Nevertheless the results suggest that Fe may also diffuse into the inner part of the spinel phase.

Initial coating evolution was shown to result from a complex interaction between oxidation of exterior Mn layer, with the formation of several Mn oxides, element diffusion and counter diffusion (Co and Mn) and alterations in alterations in crystalline structure.

References

[1] B.C.H. Steele, Solid State Ionics 129 (2000) 95–110.
[2] J.B. Goodenough, Annu. Rev. Mater. Res. 33 (2003) 91–128.
[3] K. Singh, S.A. Acharya, S.S. Bogha, Ionics 13 (2007) 429–434.
[4] J.W. Fergus, Mater. Sci. Eng. A 397 (2005) 271–283.
[5] H. Yokokawa, T. Horita, S.C. Singhal, K. Kendall (Eds.), High Temperature Solid Oxide Fuel Cells: Fundamentals Design and Applications, Elsevier, Oxford, 2003, pp. 119–147.
[6] H.U. Anderson, F. Tietz, in: S.C. Singhal, K. Kendall (Eds.), High Temperature Solid Oxide Fuel Cells: Fundamentals Design and Applications, Elsevier, Oxford, 2003, pp. 177–195.
[7] N. Shaigan, W. Qu, D.G. Ivey, W. Chen, J. Power Sources 195 (2010) 1529–1542.

[8] A. Petric, H. Ling, J. Am. Ceram. Soc. 90 (2007) 1515–1520.
[9] J. Wu, Y. Jiang, C. Johnson, X. Liu, J. Power Sources 177 (2008) 376–385.
[10] J. Wu, C.D. Johnson, R.S. Gemmen, X. Liu, J. Power Sources 189 (2009) 1106–1113.
[11] N. Shaigan, D.G. Ivey, W. Chen, J. Power Sources 185 (2008) 331–337.
[12] M.R. Bateni, P. Wei, X. Deng, A. Petric, Surf. Coat. Technol. 201 (2007) 4677–4684.
[13] K. Wang, Y. Liu, J.W. Fergus, J. Am. Ceram. Soc. 94 (2011) 4490–4495.
[14] N.J. Magdefrau, L. Chen, E.Y. Sun, J. Yamanis, M. Aindow, J. Power Sources 227 (2013) 318–326.
[15] J. Froitzheim, S. Canovic, M. Nikumaa, R. Sachitanand, L.G. Johansson, J.E. Svensson, J. Power Sources 220 (2012) 217–227.
[16] J.R. Davies (Ed.), ASM Specialty Handbook: Nickel, Cobalt and Their Alloys, ASM International, 2000, pp. 349–355.
[17] P. Wei, O.E. Hileman Jr., M.R. Bateni, X. Deng, A. Petric, Surf. Coat. Technol. 201 (2007) 7739–7745.
[18] P. Radhakrishnamurthy, K.N. Reddy, J. Appl. Electrochem. 4 (1974) 317–321.
[19] A. Brenner, Electrodeposition of Alloys – Principles and Practice, in: Practical and Specific Information, vol. II, Academic Press Inc., New York, 1963, pp. 137–156.
[20] B.D. Cullity, Elements of X-ray Diffraction, Addison-Wesley Publishing Company Inc., Reading, Massachusetts, 1956, pp. 466–468.
[21] M. Pourbaix, Atlas of Electrochemical Equilibria in Aqueous Solutions, NACE, Houston, Texas, 1974.
[22] K. Ishida, T. Nishizawa, Bull. Alloy Phase Diagrams 11 (1990) 125–137.
[23] A.N. Grundy, B. Hallstedt, L.J. Gauckler, J. Phase Equilib. 24 (2003) 21–39.
[24] K. Satomi, J. Phys. Soc. Jpn. 16 (1961) 258–266.
[25] G.F.V. Voort, H.M. James, ASM Handbook, in: Metallography and Microstructures, vol. 9, ASM Handbook Committee, ASM International, 1992, pp. 279–296.